The 2011 Mw 7.1 Van (Eastern Turkey) earthquake

J. R. Elliott,[1] A. C. Copley,[2] R. Holley,[3] K. Scharer,[4] and B. Parsons[1]

Received 28 June 2012; revised 22 December 2012; accepted 1 February 2013.

[1] We use interferometric synthetic aperture radar (InSAR), body wave seismology, satellite imagery, and field observations to constrain the fault parameters of the M_W 7.1 2011 Van (Eastern Turkey) reverse-slip earthquake, in the Turkish-Iranian plateau. Distributed slip models from elastic dislocation modeling of the InSAR surface displacements from ENVISAT and COSMO-SkyMed interferograms indicate up to 9 m of reverse and oblique slip on a pair of en echelon NW 40°–54° dipping fault planes which have surface extensions projecting to just 10 km north of the city of Van. The slip remained buried and is relatively deep, with a centroid depth of 14 km, and the rupture reaching only within 8–9 km of the surface, consistent with the lack of significant ground rupture. The up-dip extension of this modeled WSW striking fault plane coincides with field observations of weak ground deformation seen on the western of the two fault segments and has a dip consistent with that seen at the surface in fault gouge exposed in Quaternary sediments. No significant coseismic slip is found in the upper 8 km of the crust above the main slip patches, except for a small region on the eastern segment potentially resulting from the M_W 5.9 aftershock on the same day. We perform extensive resolution tests on the data to confirm the robustness of the observed slip deficit in the shallow crust. We resolve a steep gradient in displacement at the point where the planes of the two fault segments ends are inferred to abut at depth, possibly exerting some structural control on rupture extent.

Citation: Elliott, J. R., A. C. Copley, R. Holley, K. Scharer, and B. Parsons (2013), The 2011 Mw 7.1 Van (Eastern Turkey) earthquake, *J. Geophys. Res. Solid Earth*, *118*, doi:10.1002/jgrb.50117.

1. Introduction

[2] On the 23 October 2011 (10:41 UTC, 13:41 local time), a M_w 7.1 earthquake struck Eastern Turkey (U.S. Geological Survey National Earthquake Information Center (USGS NEIC) and Figure 1), just north of the city of Van (population 370,000), on the eastern edge of Lake Van (Figure 2). This earthquake resulted in over 600 deaths, largely in the city of Erciş (Figure 2, population 97,000) on the northern shore of Lake Van, on the hanging wall of the fault [*Erdik et al.*, 2012; *Daniell et al.*, 2011]. The largest aftershock (M_w 5.9, USGS NEIC) occurred just over 10 h later; although a M_w 5.7 aftershock on 9 November killed a further 40 people, largely due to additional damage in the city of Van.

[3] The largest instrumentally recorded earthquake to have struck the region before was the 1976 M_w7.1 strike-slip earthquake on the right-lateral Chaldiran Fault, 60 km north-east of Van (Figure 2), although a M 7 earthquake also struck north of Erciş in April 1903 [*Ambraseys*, 2001]. Two significant pre-instrumental earthquakes are known to have affected the immediate region of Van in the last few centuries, estimated to be in the upper magnitude 6 range [*Ambraseys*, 1989]. On 8 March 1715, domes on churches in both Van and Erciş collapsed in a severe earthquake at dawn [*Ambraseys and Finkel*, 1995]. A more destructive earthquake occurred around 1646–1648 in the region to the southeast of Lake Van [*Albini et al.*, 2012], seriously damaging the town of Van and resulting in collapse of churches, mosques, and part of the citadel [*Ambraseys and Finkel*, 1995].

[4] The Turkish-Iranian Plateau, in which the region around Van is situated, is the result of the ongoing collision of Arabia and Eurasia (Figure 1b), with a current overall north-south convergence rate of 23 mm/yr [*Reilinger et al.*, 2006]. In the east, the convergence with Iran has created the Zagros mountains, and to the north the Greater Caucasus lie between the Black and Caspian Seas, both in zones of distributed deformation. To the west, more microplate-like motion of Anatolia occurs along the strike-slip North and East Anatolian Faults. Plate circuit reconstructions of the Eurasia-Arabia collision by *McQuarrie et al.* [2003] suggest the overall convergence rate has been fairly constant

All supporting information may be found in the online version of this article.

[1]COMET+, Department of Earth Sciences, University of Oxford, Oxford, UK.
[2]COMET+, Department of Earth Sciences, Bullard Laboratories, Cambridge, UK.
[3]CGG NPA, Edenbridge, Kent, UK.
[4]USGS, Pasadena, California, USA.

Corresponding author: J. R. Elliott, COMET+, Department of Earth Sciences, University of Oxford, Parks Road, Oxford OX1 3PR, UK. (john.elliott@earth.ox.ac.uk)

2169-9313/13/10.1002/jgrb.50117

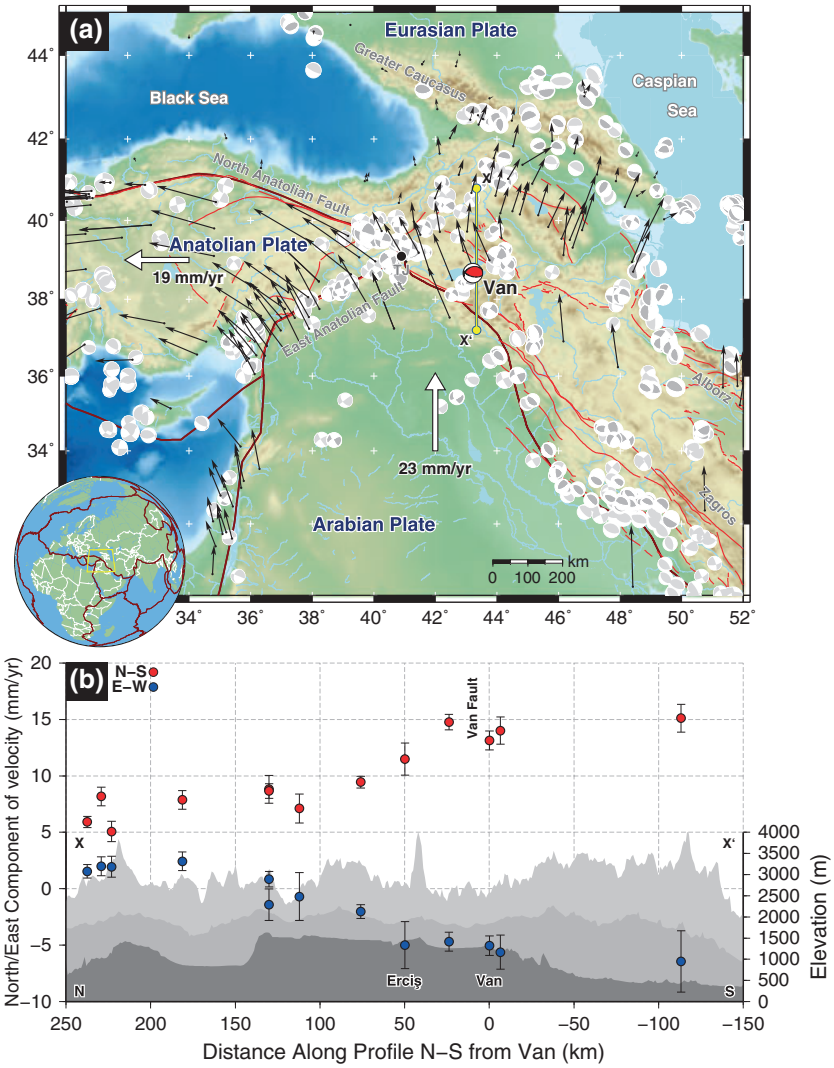

Figure 1. (a) Seismotectonic map of interaction between the Arabian, Eurasian, and Anatolian plates centered on Eastern Turkey. Relative plate convergences are marked by white arrows, calculated from *DeMets et al.* [2010] and plate boundaries (dark red) are from *Bird* [2003]. Earthquake focal mechanisms are from a compilation by *Copley and Jackson* [2006] (dark grey) and from the GCMT catalogue (light grey) M_w5.5+ for the period 1976–2010 [*Ekström et al.*, 2005]. The body wave focal mechanism for the 2010 Van earthquake is shown in red. GPS vectors (black arrows) are from a compilation by *Reilinger et al*. [2006], relative to a stable Eurasia. Major faults (red lines) for the region of Turkey are from *Şaroglu et al.* [1992], and for Iran from *Walker et al.* [2009]. TJ denotes the location of the Karliova triple-junction 150 km WNW of Van. (b) Profile running north-south through Van of GPS velocities [*Reilinger et al*., 2006] projected onto the profile with a Northern component (red circles) and Eastern component (blue circles) shown. GPS sites are taken from a swath 75 km wide to the East and 125 km wide to the West of the line marked X–X′ in Figure 1a. Also shown are maximum (light grey), mean (grey), and minimum (dark grey) topographic profiles for the same swath window.

between 2 and 3 cm/yr for the past 56 Ma, and the direction of convergence has been northward since 25 Ma (being north-eastward prior to this).

[5] The change in the rate of convergence in the immediate region of this part of Eastern Turkey can be seen by taking a 200 km wide swath profile of GPS velocities [*Reilinger et al*., 2006] N through Van. A significant decrease in the northward component of velocity from around 15 to 5 mm/yr occurs over a distance of 250 km, with the rate of convergence across the Van fault being less than 5 mm/yr (Figure 1).

[6] At the longitude of the Greater Caucasus, the convergence between Arabia and Asia is accommodated by sub-parallel right-lateral strike-slip faulting within the Turkish-Iranian Plateau, and thrust faulting in the Greater Caucasus [*Jackson*, 1992]. In addition, a band of thrust faulting extends from the Karliova triple-junction (Figure 1), where the North and East Anatolian Faults meet, eastward into the interior of the Turkish-Iranian Plateau [*Copley and Jackson*, 2006]. This band of thrusting has produced large earthquakes in 1966 (the Varto earthquake) [*Ambraseys and Zátopek*, 1968; *McKenzie*, 1972]

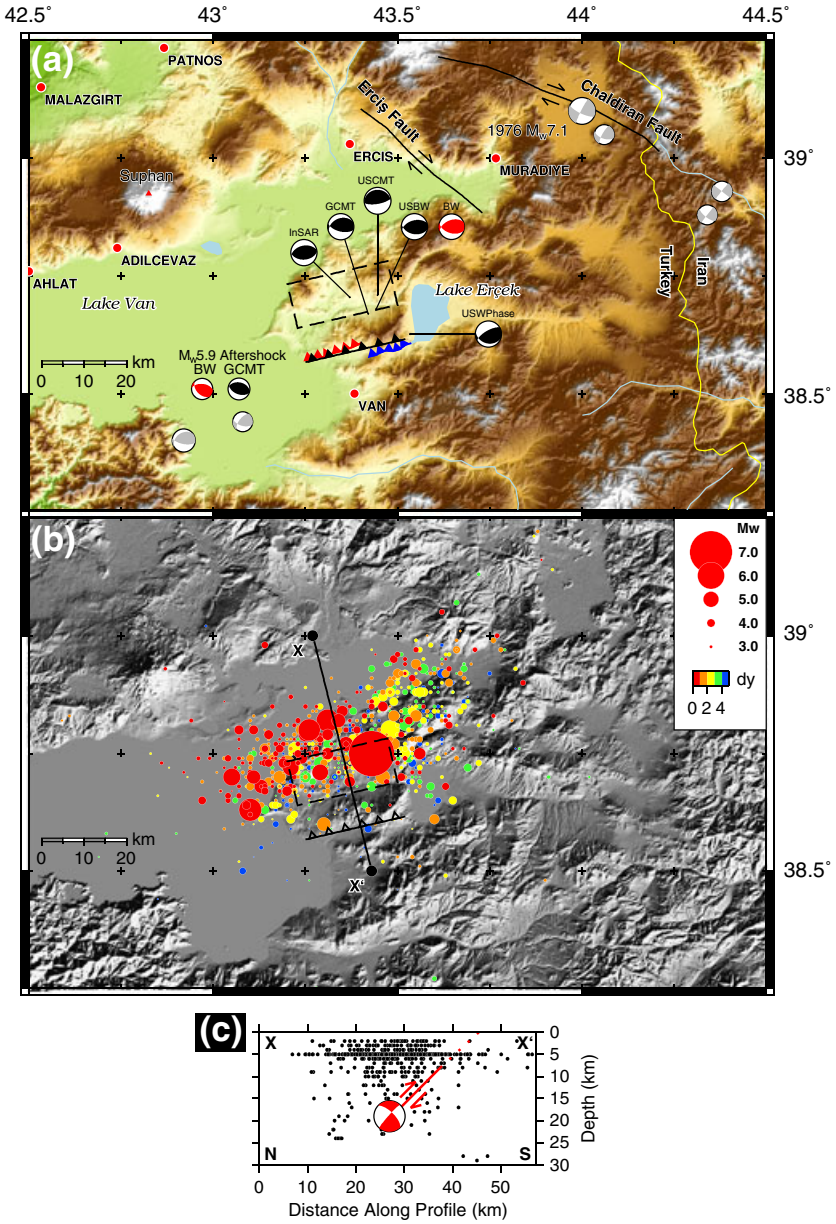

Figure 2. (a) Elevation map of the area around the city of Van with focal mechanisms (black) of the 23 October 2011 event from the USGS and GCMT (offset from actual location by a black line), and the body wave solution from this study (red). Also included are the body wave and GCMT solutions for the aftershock 10 h after the mainshock. Grey focal mechanisms are from the compilation by *Copley and Jackson* [2006]. The black barbed line indicates the up-dip projection of the single fault segment model to the surface, and the dashed box represents the surface projection of the outline of the fault that ruptured at depth. The red line marks the trace of the surface rupture mapped by *Akyuz et al.* [2011], whilst the blue line marks their fault trace based upon the geomorphology. Previous fault traces are from *Şaroglu et al.* [1992]. (b) Aftershocks in the 5 days following the mainshock, from the European-Mediterranean Seismological Centre (EMSC), scaled in size by magnitude and colored by the number of days after the mainshock. (c) Cross-section through X–X′ shown in Figure 2b of aftershocks with the body wave solution superimposed on the depth extent of rupture marked by a red line found from modeling the InSAR observations. The dotted line indicates the up-dip surface projection of the fault plane, which outcrops less than 10 km from the city of Van.

and in 2000 (thrust faulting beneath Lake Van, 40 km to the south-west of the event we discuss here [*Copley and Jackson*, 2006]).

[7] It is well known that following a large earthquake, the along-strike unruptured portions of the fault system are usually brought closer to failure and are more likely to fail [e.g., *King et al.*, 1994]. The possibility of similar-sized earthquakes occurring in almost the same epicentral location relatively soon after the first (i.e., before a typical seismic cycle would be complete) due to segmentation

of the fault with depth is less well documented. This scenario was shown to be the case for two *Mw* 6.2 reverse faulting events which occurred 10 months apart in 2008 and 2009 at almost the same location in the Qaidam basin, China [*Elliott et al.*, 2011]. Similarities between the Van earthquake and the deeper reverse faulting Qaidam event in 2008 that was followed by the up-dip shallow rupture of the same magnitude the following year raise concern for future seismic hazard near Van. Amplifying this concern, the upper and significantly wide part of the fault segment appears to be potentially seismogenic based upon fault scarp geomorphology and presence of fault gouge at the surface, assuming that shallow displacement is not accommodated by stable creep.

2. Fault Geometry

[8] In this study, we principally use SAR data from COSMO-SkyMed and ENVISAT to form interferograms of the ground displacement due to the earthquake. From these measurements, and using constraints from field observations and satellite imagery, we determine the geometry of faulting and the depth distribution of slip. We perform a body wave seismological solution to form an independent estimate of the earthquake mechanism and centroid depth.

2.1. Field Observations and Satellite Imagery

[9] We use WorldView-2 imagery from before the earthquake (50 cm resolution), field observations, a 30 m ASTER

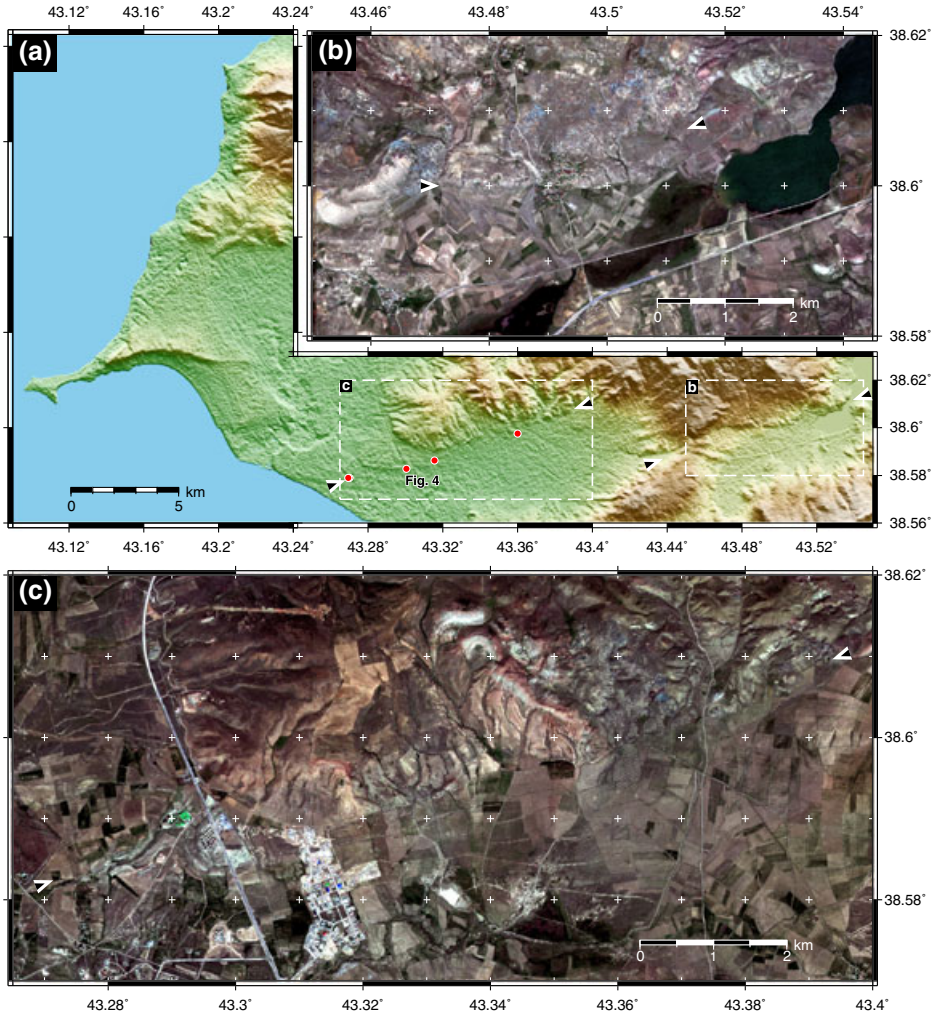

Figure 3. (a) The ASTER GDEM (30 m shaded relief) of the epicentral region indicating the fault scarps and lake terraces in the geomorphology. Red circles denote the locations of small ground ruptures mapped in the field. Black arrows indicate the extent of straight line segments used to approximate the faults used in the modeling. ASTER GDEM is a product of METI and NASA. (b) World-View 2 imagery of the pre-earthquake (May 2011) view of the eastern fault segment (standard bands RGB, pan-sharpened to 50 cm resolution). Arrows indicate the location and strike of the scarp. The surface geomorphology for this segment is not as clear as for the western segment along which surface cracks were found in the field, but the high topography here suggests a fault trace that is further south at this location. There is similar topography at the scarp, but shorter, less continuous sections. (c) World-View 2 imagery of the western fault segment. The surface geomorphology of the fault scarp is more clear on this segment, with an obvious change in incision moving NW across the fault.

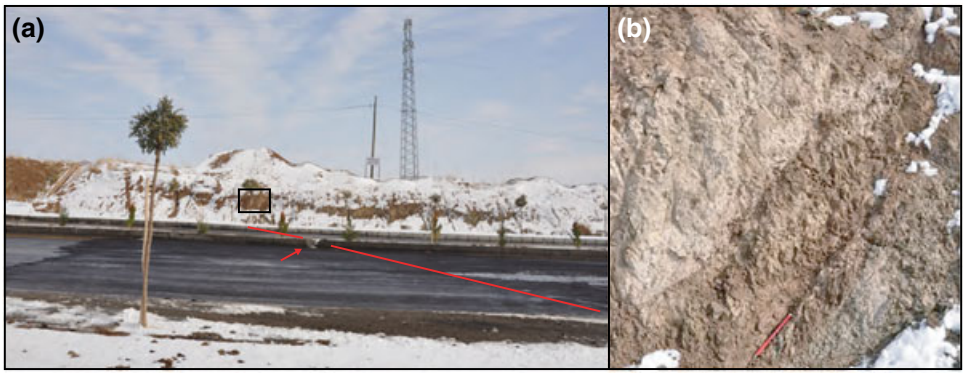

Figure 4. (a) View east of repaired tarmac road at fault lineament. Red line connects locality of fault gouge in road cut (black box) and broken curbs at N38.5826°, E43.300°. (b) Outcrop of fault gouge dipping 45°–50° to the north, 15 cm pencil for scale. Hanging wall deposits are Pleistocene lake beds.

DEM, and Turkish geologic map to examine the tectonic geomorphology of the region (Figure 3). (At the time of writing no suitable post-earthquake high-resolution scenes existed that were not significantly degraded by cloud/snow cover.) Along the western segment of the fault, the surface expression of past faulting is manifest as short, anastomosing fault scarp segments, characteristic of splays from imbricate thrust faults. The scarps cut through Plio-Pleistocene lake terraces which are incised in the uplifted (northern) block (Figure 3). The range-front fault morphology for the eastern segment is more complex as bedrock (Cretaceous ophialitic melange) and possible large landslides, rather than young terraces, dominate the terrain and make recency of faulting less clear.

[10] In the field, we observed sparse, small magnitude ground deformation that, in combination with other post-earthquake reports [*Akyuz et al.*, 2011; *Emre et al.*, 2011; *of Turkey Prime Ministry Disaster and Department*, 2012], maps out a 11.6 km lineament trending 255° from the shore of Lake Van, at the base of a low range north of Van (Figure 3). Most of the deformation was seen in brittle, man-made structures, largely irrigation canals and roads and indicated up to 10 cm of slip (Figure 4). The sense of slip was typically compressional, with an ∼10 : 4 ratio of thrust to horizontal slip, but varied in magnitude and sense of slip along strike, in some places reflecting tilting and rotation of the ground surface (for example, tensional cracks at the top of a scarp produced by rotation of the scarp riser). *Akyuz et al*. [2011] observed ground deformation in natural surfaces as narrow cracks and mole tracks a few centimeters high but hundreds of meters long at two locations along the lineament, but these were erased by rain and snow following the earthquake. Where this lineament crossed a 3 m high road cut, a north dipping, 45°–50° gouge zone sheared Late Pleistocene lake deposits (Figure 4).

2.2. Teleseismic Body Wave Modeling

[11] We use teleseismic body waveform modeling to obtain independent estimates of the source parameters and centroid depth for the M_w 7.1 Van mainshock and M_w 5.9 aftershock. The methodology is well established and we describe it only briefly in the Supporting Information. The fault parameters are given in Table 1 and the minimum misfit solutions for *P* and *SH* waves are given in Figure 5 for the mainshock and Figure S1 for the largest aftershock.

[12] The body wave solution for the mainshock is consistent with that from GCMT and the USGS (Figure 2), indicating slightly oblique ENE-WSW striking, high angle reverse faulting, with a centroid depth of 20 km, and a moment magnitude of 7.0. Permitting a tolerance of up to 15% increase in misfit to the waveforms constrains the centroid depth to the interval 15–22 km (Figure 6). The aftershock 10 h later has a similar mechanism (Figure S1), but a shallower centroid at 10 km and a M_w of 5.8, less than 2% of the mainshock moment (Table 1).

2.3. InSAR-Derived Slip Distribution

[13] We use InSAR phase measurements from a descending interferogram from the COSMO-SkyMed X-band SAR and a pair of descending C-band interferograms from the ENVISAT satellite (Table 2). The methodology used to generate the interferograms, downsample the interferogram, data and determine the fault geometry assuming uniform slip is described by *Wright et al.* [2004] and *Elliott et al.* [2012]. From this result, we subdivide the segments into an array of subfaults following the method outlined by *Funning et al*. [2005] to form a distributed slip model. These methods are well established and are described in the Supporting Information. We neglect the contributions of any aftershocks as they all have magnitudes less than 6 (i.e., seismic moments 50 times less than the mainshock). The second COSMO-SkyMed acquisition was just 4 h after the earthquakes, so postseismic contributions will be minimized.

[14] The COSMO-SkyMed data cover only the near-field of the earthquake deformation. However, based upon the closure of the fringes (Figure 7) and comparison to the ENVISAT displacements, they cover both peaks of maximum motion toward and away from the satellite in the hanging and footwalls of the fault (96 cm and –11 cm, respectively). This is in addition to giving an almost continuous and dense coverage across the up-dip projection of the fault to the surface, where the gradients in phase are the greatest (as demonstrated by the tight fringes seen in Figure 7). Conversely, the ENVISAT pair of descending interferograms cover the far-field deformation, but have poorer coverage of the near-field due to poorer interfero-

Table 1. Fault Parameters for the Van Mainshock and Its Largest Aftershock Derived from InSAR Phase Measurements, Teleseismic Body Wave Modeling, and the Best Double-Couple Solutions in the Seismic Catalogues (GCMT, USGS)[a]

Solution	Strike °	Dip °	Rake °	Slip m	Lon °	Lat °	Length km	Width km	Top Depth km	Bottom Depth km	Centroid Depth km	Stress Drop MPa	Moment 10^{18} Nm	Magnitude M_w	Slip Vector °	P Axis Azimuth °
Van 23 October 2011 M_w 7.1 Mainshock, 10:41 UTC																
InSAR-1f	258	45	83	3.7	43.3858	38.5915	24.2	15.4	8.6	19.6	14.1	4.9	44.4	7.0	178	173
1σ	±1	±1	±2	±0.1	±0.15 km	±0.12 km	±0.2	±0.5	±0.2	±0.3	±0.2	±0.3	±1.0			
InSAR-2f-E	254	40	64	3.3	43.499	38.602	12	16.6	8.3	19.1	13.7	4.1	21.3	6.8	197	182
1σ	fixed	±1	±1	±0.2	fixed	fixed	fixed	±1.0	±0.2	±0.6	±0.3	±0.4	±0.4			
InSAR-2f-W	254	55	93	6.7	43.329	38.593	12	8.9	10.2	17.4	13.8	16.2	23.1	6.8	159	162
1σ	fixed	±1	±2	±0.9	fixed	fixed	fixed	±1.2	±0.3	±0.7	±0.2	±4.5	±0.7			
InSARFixλ	254	40/54	64/93	3.3			28	15	8	22	15		46	7.0		
BW(this study)	243	50	60								19		32.6	6.9	195	174
USGS-BW	255	50	73		43.442	38.681					20		64	7.1	190	177
USGS-CMT	272	19	101		43.354	39.451					16		99	7.3	170	173
GCMT	246	38	60		43.40	38.64					12		63	7.1	194	177
Van 23 October 2011 M_w 5.9 Aftershock, 20:45 UTC																
BW(this study)	276	52	59								9		0.59	5.8	230	207
USGS					43.20	38.63					9			5.9		
GCMT	281	40	82		43.07	38.51					12		1.1	6.0	202	198
Van 9 November 2011 M_w 5.7 Aftershock, 19:24 UTC																
USGS-CMT	269	59	–171		43.229	38.429					5		0.45	5.7		127
GCMT	267	72	179		43.28	38.30					13.5		0.43	5.7		130

[a]The apparent average static stress drop ($\Delta\sigma$) is calculated from the segment moment M_0, width W, and length L using the relation $\Delta\sigma = 2M_0/(\pi W^2 L)$ [*Scholz*, 2002]. The fault length, width, and average slip for the InSAR distributed slip with fixed rake solution are approximated by taking a rectangular fault area which incorporates the 1 m contour of the two main slip regions shown in Figure 9b. Errors stated for the InSAR uniform slip models are 1 sigma values from the result of Monte Carlo error analysis (Figure S2). The latitude/longitude locations for the faults are the centroid for GCMT, the Preliminary Determined Epicenter (PDE) for the USGS Body Wave solution (USGS), and the center of the up-dip projections of the fault segment to the surface for the InSAR solutions.

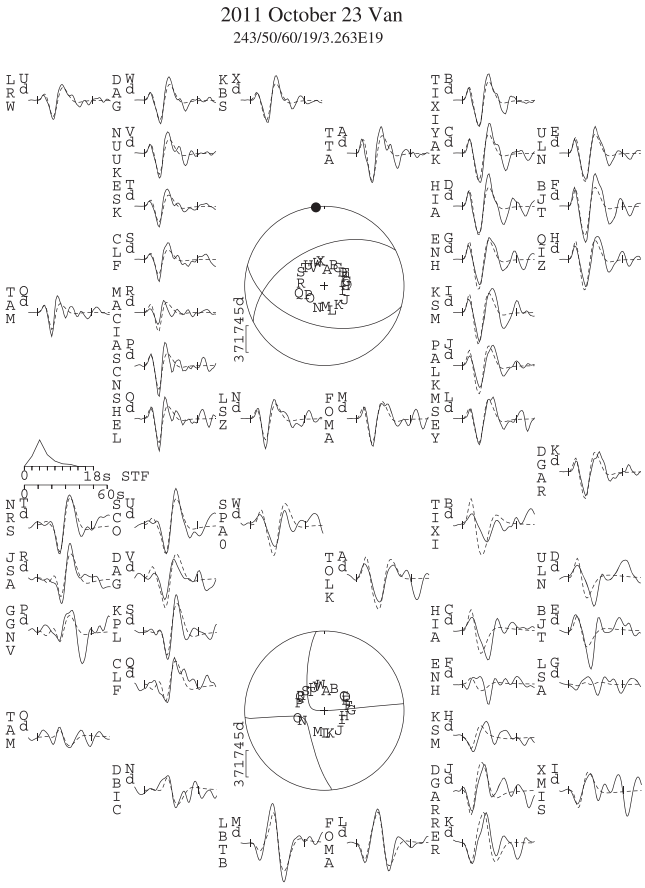

Figure 5. Van body wave minimum misfit solutions from the inversion of *P* and *SH* body waves for a point source in a half-space. Focal mechanisms show *P* (top) and *SH* (bottom) nodal planes in a lower hemisphere projection. Closed and open circles represent the *P* and *T* axes, respectively. Waveforms for each station are plotted around the focal mechanisms in approximate azimuthal locations. Observed waveforms are solid and synthetic waveforms are dashed, whilst the vertical ticks mark the inversion window. The station code is to the left of each waveform, in vertical capital letters. The vertical bar and number beside each focal sphere are the amplitude scale for the plotted seismograms (in μm). The STF is the source-time function, and the scale bar below it is the horizontal scale for the seismograms. The numbers in the header are strike, dip, rake, centroid depth (km), and moment (Nm) for the best fit solution.

metric coverage resulting from large spatial and temporal baselines (Figure 8).

[15] The smooth, continuous phase gradients and closed fringes of the InSAR data indicate the source is buried with little, if any, slip reaching the surface. We initially model the source as a single rectangular uniform slip patch and seek to find the strike, dip, rake, and location of the fault that best fits the InSAR data. The inferred fault geometry is shown in Table 1, and the modeled fault trace and outline are shown in Figures 2 and 7, with comparison made to the seismological mechanisms.

[16] From this simple model, we find an WSW-striking 23 km long fault-plane solution, dipping to the NNW with a centroid depth of 14 km and a moment magnitude of 7.1. The uniform slip value is 3.8 m and remains buried, with an upper limit of 8 km below the surface. The motion is predominately reverse, with a small strike-slip component in the left-lateral sense. The body wave solution (Figure 5) differs in strike and rake by about 15°–20°, with a 5 km deeper centroid and ∼30% smaller moment, but similar dip of 50° for the NNW dipping plane. The misfit well for the body wave solution is shallow in the range 15–20 km for the centroid depth (Figure 6), and the moment values match more closely between the InSAR and seismological solution for depths around 14 km.

[17] The up-dip fault plane location and strike project to the surface 10 km to the north of Van (Figure 2) and agree approximately with the general strike of the range-front scarp visible in satellite imagery. The field observations of ground deformation along the range front have a strike of 255°. The InSAR-derived strike is almost identical (258°), but extends another 12 km to the east of the surface observations of faulting, for a total length of 24 km.

[18] Given the spatial similarities between the range-front morphology and the 4 km southward step in the COSMO-SkyMed displacement field between the western and eastern halves of the surface trace (Figure 7), we increase the complexity of the source by modeling the earthquake as a rupture on two distinct fault segments. This also permits the top depths of rupture to vary from the west,

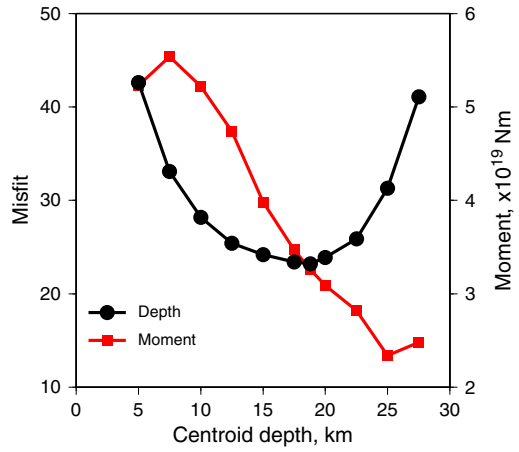

Figure 6. Body wave misfit versus centroid depth. The minimum misfit is at 19 km, but the increase in misfit to the seismograms is less than 15% over the depth interval 15–20 km. The trade-off in moment with depth is shown by the red line.

where the ground cracking was documented, to the east, where no evidence of surface rupture was evident. We fix the location and lengths of these two segments to the surface trace in the case of the western segment, and the fault geomorphology for the eastern segment. We then solve for the fault dip, rake, top, and bottom depths on each segment as before. Slip on both segments still remains buried beneath 8 km depth (Table 1). The western portion dips more steeply (54°) to the NNW and is pure reverse, whilst the eastern segment dips at 40° and has more oblique slip, but both have a similar magnitude. The centroid locations and moment tensors compared to those from the seismological catalogues are given in Table 3. Locations differ by about 5 km and the centroids by 2 km.

[19] We extend the two fault segments along strike and down-dip to solve for the distribution of slip on the planes using 1 km long by 1 km wide subfault patches, following the procedure outlined in the Supporting Information. The resulting slip distribution is shown in Figure 9, with the models and residuals to the three interferograms shown in Figure 8 (downsampled data, model and residual points are shown in Figure S3). The slip values and errors are given in the Supporting Information (Tables S1–S4). The pattern is dominated by two regions of slip, with peak motion up to about 9 m on each. The strongest requirement for two segments is seen in the sharp 4 km right-step in the fringes of the COSMO-SkyMed data, most obvious at the transition from the hanging wall to the footwall (Figure 8), which can only be matched with a pair of faults. High gradients in slip are found at depths of 9–11 km. The fault rupture area largely occupies the same lateral and depth extents as for the uniform slip model. Ninety percent of the total moment is constrained to the depth range 9–20 km. Some slip is modeled to occur on the deeper portion of the eastern fault below 20 km (Figure 10), although the errors indicate the magnitude of slip in this region is not well constrained. Short wavelength residuals up to about 7 cm remain in the COSMO-SkyMed in the hanging wall (Figure 8c), and longer wavelength residuals remain in the ENVISAT interferograms associated with orbital and atmospheric errors (Figures 8f and 8i).

[20] We note that the slip in the model (Figure 9) quickly tapers off up-dip at about the depth (10 km) at which the upper corner ends of two fault planes meet (Figure 10) due to the difference in their dips and relative positions. Very minor slip is found in the upper 8 km (equivalent to 9–11 km in down-dip fault width in the models). Predicted surface offsets from the top 1 km of the fault model indicate at most 0–20 cm of near-surface slip along the fault trace, consistent with surface observations. At the eastern end of the eastern segment, up to 40 cm of slip is modeled, but this is immediately beneath lake Erçek where no InSAR surface displacements are retrievable and therefore the slip is unconstrained.

[21] The fit of the model to a profile of the COSMO-SkyMed data taken perpendicular to the fault is shown in Figure 8. The minimum elevation profile along this same profile has a distinctive asymmetric concavity at the intersection of the fault trace with the surface just north of Van (Figure 8). The minimum-elevation profile records the interplay between the river downcutting and the fault hanging wall uplift. The steep and rougher relief front of the ridge topography on the south side is likely to be due to uplift along the range-front scarp, while the longer wavelength concave profile to the north across the drainage divide results from fluvial incision keeping pace with tectonic

Table 2. Details of Interferograms for the M_w 7.1 23 October 2011 Van Earthquake[a]

Satellite	Track	Direction	Incidence	Master	Slave	ΔT	ΔPT	$B_\perp$	σ^2	Distance	Data	Weight	RMS (cm)		
	#	asc/dsc	°	yymmdd	yymmdd	days	days	m	cm^2	km	pts		uniform	fix λ	single plane
Coseismic Acquisitions															
CSM		dsc	28	111010	111023	13	0	192	0.34	5.1	2010	1	3.0	2.1	2.6
ENV	121	dsc	41	101105	111031	360	8	138	0.12	4.1	2030	1	1.9	1.4	1.4
ENV	394	dsc	41	110722	111119	120	27	221	0.97	6.2	2007	1	2.5	2.3	2.3
Postseismic Acquisitions															
CSM		dsc	28	111023	111026	3	0	306	0.52	2.6	2216	1		1.1	
ENV	394	dsc	41	111119	111219	30	27	71	0.55	5.9					

[a]Columns show COSMO-SkyMed/ENVISAT tracks, satellite directions (all descending), incidence angle (°) in the center of the scene, dates of SAR frames, time interval ΔT, postseismic interval ΔPT, and perpendicular baseline $B_\perp$. The perpendicular baseline is the average of the top and bottom perpendicular baseline in the interferogram. The variance (σ^2) and *e*-folding length scale (distance) are those calculated from the covariance function of interferogram noise and are used in the Monte Carlo estimation of fault parameter errors. The number of data points used in the inversion, the relative weighting for each of the data sets, and the weighted RMS for the uniform slip and distributed slip (fixed rake λ and single deep plane) inversions are also given.

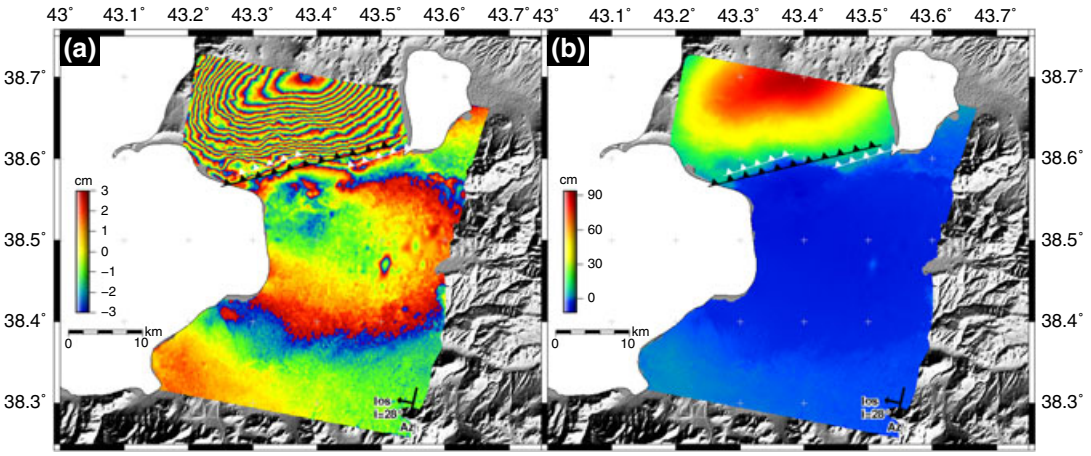

Figure 7. (a) The COSMO-SkyMed interferogram formed from an acquisition 13 days prior to the earthquake and one just 4 h after the event. The displacement points in the interferogram have been interpolated to form a continuous surface for clarity. Colors show range changes as fringes re-wrapped to 6 cm, with the color cycle blue to red indicating increasing motion away from the satellite for the three satellite tracks. The single fault segment is marked by a solid black line, the pair of segments by white lines. Satellite track azimuth (Az) and line-of-sight (LOS) with angle of incidence (i) are shown by black arrows. (b) Unwrapped COSMO-SkyMed interferogram. The peak line-of-sight displacement is 94 cm toward the satellite and 12 cm away from the satellite.

uplift. A similar but larger amplitude version of this asymmetric concave profile is seen in the mountains to the south of Van, possibly indicating a similar fault structure there, which also has a similar WSW strike in the topography (Figure 2).

3. Slip Depth-Extent Tests

[22] Given that this event is buried and the elastic lid of the upper crust will act as a filter on the fault slip relative to the surface deformation observed, we test the ability of the InSAR measurements to resolve the depth extent of faulting. A deeper fault source makes it more difficult to resolve the distribution of slip, resulting in finite fault area dislocations appearing more like line or point sources [*Lohman and Simons*, 2005a; *Page et al.*, 2009]. Consequentially, deeper sources have a focal plane ambiguity in the geodetic solution in the same way as do the seismological solutions. It is important to address these limitations in assessing the depth extent of faulting and potential future seismic hazard for Van.

[23] Several approaches exist to assess the resolution in slip permitted from the use of surface displacements whereby the density of data sampling and the size of subfaults in the model are varied [e.g., *Fialko*, 2004; *Lohman and Simons*, 2005b; *Page et al.*, 2009; *Atzori and Antonioli*, 2011]. We address the reliability of depth extent of faulting by first examining the RMS cost for different a priori fixed choices of upper top fault depths and assessing the trade-off with other fault parameters, and second by performing checkerboard tests using known slip distributions, forward modeling the resulting displacements at the data sample locations and using this as synthetic input to the slip inversion. We also examine the postseismic interferograms to see if significant early afterslip has occurred on the shallow portions of the fault.

3.1. Fault Parameter RMS Wells

[24] Our first test is to introduce a region of lower slip magnitude above the deeper high-slip segments for our rectangular uniform slip models (whose parameters are kept fixed to those given in Table 1) to test how much slip could also have reasonably occurred in the uppermost crust to the surface. The misfit in terms of the root mean square of the residuals to the InSAR data increases significantly once more than a few tens of centimeters of slip is introduced on the shallow portion of the fault (Figure 11a).

[25] We also explore the change in the misfit to the InSAR data resulting from fixing the top depth at 1 km intervals for each segment in turn while holding the other fault parameters (apart from slip) fixed to those found in Table 1 for our uniform slip models. The well-defined minimum misfit is at 9–10 km, with a significant increase in RMS seen as we attempt to force the slip to approach the surface on either segment (Figure 11). For deeper upper rupture depths, the RMS misfit increases (although not quite as steeply), but the slip-to-width ratios become physically unrealistic as the fault plane collapses to a line source.

[26] We also investigate two parameter RMS wells for the top depth of faulting versus the other eight faulting parameters (Figure S4), for each of the pair of segments in turn. The shape of these misfit wells indicates that the upper rupture depth is strongly bounded at 8–10 km and that the upper depth on either segment does not trade off significantly enough with any of the other fault parameters to permit near surface slip.

3.2. Checkerboard Tests

[27] Using the fault geometry of the two segments determined from uniform slip modeling, we forward-model known checkerboard slip distributions with a range of subfault patch sizes from 2 to 9 km, with alternating slip

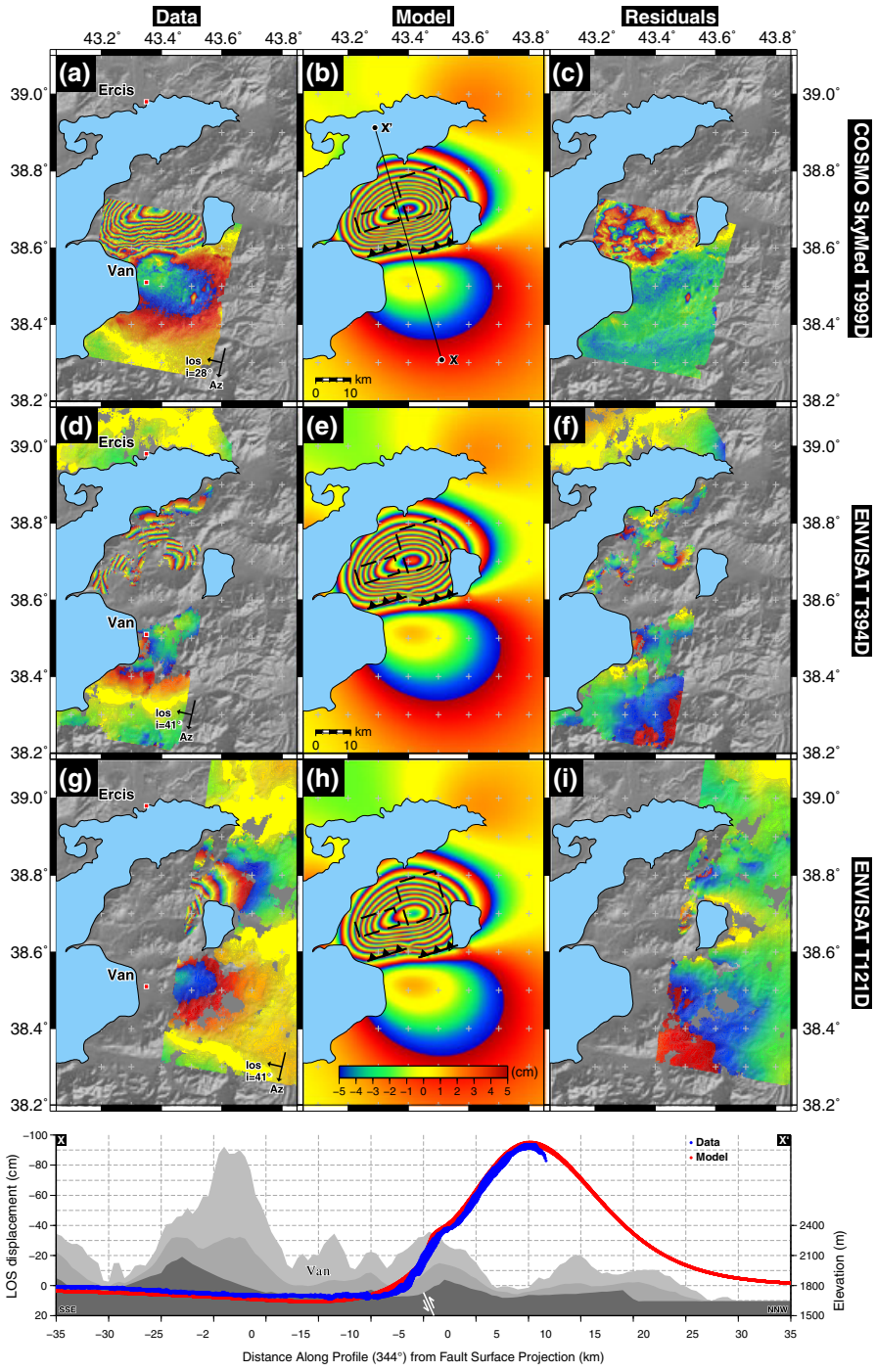

Figure 8. Interferograms, models, and residuals based upon distributed slip modeling for the Van earthquake for the three satellite tracks. Colors show range changes as fringes re-wrapped to 10 cm, with color cycles blue through yellow to red indicating motion away from the satellite. The up-dip projection of the fault segments are marked by the pair of barbed solid lines (triangles on the hanging wall), the surface outline of the uniform slip regions by dashed rectangles. The satellite track azimuths (Az) and line-of-sight directions (LOS) with angle of incidence (i) are indicated by black arrows. Profile X–X′ through the COSMO-SkyMed data, model, and topography is shown at the bottom. The profile is taken perpendicular to the strike of the fault segments. InSAR displacements are represented by blue dots, the modeled data projected into the same line-of-sight by red dots, sampled along a 70 km long profile in a 2 km wide swath. Profiles of topography are taken from the SRTM 3 s data along the same sections, sampling 10 km wide swaths and showing minimum (dark grey), mean (grey), and maximum (light grey) elevations. The Karasu River cut the broad valley centered below the peak uplift. The line-of-sight displacement axis has been inverted so negative motion (which is toward the satellite and mainly uplift in this case), is to the top of the figure.

Table 3. Full Moment Tensors from Seismology and InSAR[a]

Source	Lon. °	Lat. °	Depth km	M_{rr} 10^{19}Nm	M_{tt} 10^{19}Nm	M_{pp} 10^{19}Nm	M_{rt} 10^{19}Nm	M_{rp} 10^{19}Nm	M_{tp} 10^{19}Nm	M_0 10^{19}Nm	DC %
InSAR	43.366	38.708	13.7	3.658	–3.619	0.0382	–0.2227	–0.6825	0.5976	4.38	98
GCMT	43.40	38.64	12.0	5.270	–5.860	0.591	2.130	–1.780	–0.612	6.27	100
USGS	43.446	38.710	16	5.89	–6.13	0.24	7.73	1.60	–0.51	9.9	97

[a]The six components of the moment tensor (M_{rr}, M_{tt}, M_{pp}, M_{rt}, M_{rp}, M_{tp}), and the total moment M_0 are given. The InSAR moment tensor is calculated from summing the two uniform slip segments in Table 1. We calculate the percentage double-couple component DC of the InSAR and seismological solutions following a definition given by *Jackson et al.* [2002], where a pure double-couple source (with eigenvalues λ of –1, 0, 1) is 100% and a compensated linear vector dipole (e.g., $\lambda = -1/2, -1/2, 1$) is 0%. $DC = 100*\{1 - [(3*|\lambda_2|)/(|\lambda_1| + |\lambda_3|)]\}$.

values of 0 and 2 m (Figure 12). These forward models are then masked to the same locations for which we have coherent unwrapped InSAR data on each of the tracks, but with no noise added to the synthetics as we are testing the effect of data sampling only. The modeled displacements are then downsampled using the same quadtree approach as described in the Supporting Information, to give the same input data distribution and number of displacement points.

[28] The results show regions of the distributed slip fault plane on which the heterogeneity of slip can be resolved, and to what degree this slip is smoothed vertically and laterally. While this is an artificial scenario regarding the slip distribution, it is particularly useful in demonstrating where large gradients of slip down to zero can be resolved. The decreased resolution with depth is apparent in all cases, as the elastic crust filters the deformation due to slip patches (Figure 12). Only features of at least 3 km width are resolvable at 5 km depth and only 6 km scale features of slip resolvable down to 10 km. In the depth range 10–20 km, the limit is 9+ km. However, we can be confident that the sharp gradient in slip observed in our model at 10 km depth (Figure 9) is resolvable as it occurs along a segment greater than 6 km in size.

3.3. Postseismic Deformation

[29] We have examined COSMO-SkyMed and ENVISAT postseismic images (Table 2) to address whether significant aftershock deformation or postseismic afterslip has occurred on the shallow portions of these fault segments. A pair of 6 cm fringes is observed in the COSMO-SkyMed data covering the period from 4 h to 4 days after the earthquake over the region of the eastern segment (Figure 13a). Modeling this COSMO-SkyMed interferogram for afterslip using the orientation of two fault segments from the main earthquake reveals a significant shallow slip patch of about half a meter, located between 5 and 10 km depth (Figure 13d). The equivalent moment magnitude is about M_w 5.9, which is the same magnitude as the largest aftershock which occurred 10 h after the mainshock (Table 2) and is covered by this postseismic interferogram. Therefore, this small patch of significant slip (up to 70 cm) could be due to seismic slip of the aftershock on the shallow portion of the fault plane.

[30] A discontinuity in the interferometric phase is also observed in the COSMO-SkyMed data for the western portion of the fault (Figure 13a). The jump in phase of about 5 cm is located and aligned along the center of this western fault segment, consistent with minor near-surface afterslip found in the field. There is little afterslip modeled on the shallow parts of this fault segment (Figure 13d).

[31] We examined a COSMO-SkyMed interferogram covering the postseismic period from 4 days to 1 month after the earthquake, but widespread decorrelation due to snow fall in the area resulted in this interferogram being of limited use. However, the ENVISAT postseismic interferogram covering the period from 1 to 2 months after the main earthquake (Figure S5) shows no significant afterslip on the fault planes (except directly beneath Lake Erçek where 50 cm of slip is modeled but is potentially due to noise from the lack of surface deformation constraint here).

4. Discussion

4.1. Short-Term Uplift

[32] From the distributed slip model, we can calculate the instantaneous vertical component of surface displacement due to this earthquake (Figure 14). The region of uplift associated with this reverse faulting event is centered on the area north of the city of Van and shows a slight asymmetry, with a southern flank that is steeper and narrower than the northern. This pattern is weakly reflected in the topography of the mountains north of Van, which show a steep southern flank and a northern edge that descends more gently below Lake Van (Figure 8). The long axis of the uplift pattern is parallel to generalized fold axes mapped by *Altinli* [1966] and aligned with a peninsula that protrudes in a west-south-westerly direction into Lake Van (Figure 14a).

[33] Overall, the pattern from this earthquake is consistent with folding by limb rotation during fault propagation folding [*Mitra*, 1990], in which case the small surface displacements mapped in the field could be the product of bending of an axial surface up-dip of the fault, rather than coseismic slip on the fault plane (sensu stricto). The eastern half of the western segment is characterized by subdued, anastomosing lineations that are likely fault scarps. Paleoseismic trenching across the fault segments would resolve how frequently previous earthquakes had larger coseismic ruptures extending all the way to the surface.

[34] Lacustrine terraces, originally mapped by *Schweizer* [1975] and further studied and dated by *Kuzucuoğlu et al.* [2010], reveal a complex lake level history for Lake Van, modulated largely not only by climate, but also by changes in sill elevations due to volcanic flows and local changes in terrace elevations due to tectonic activity. The western fault mapped in this study is sub-parallel to and crosses a set of major aggradational terraces (Figure 14c) (elevations 1700 and 1726 m above sea level) that were deposited between 100 and 22 ka [*Kuzucuoğlu et al*., 2010]. The continuation of these surfaces around the eastern shore of Lake Van

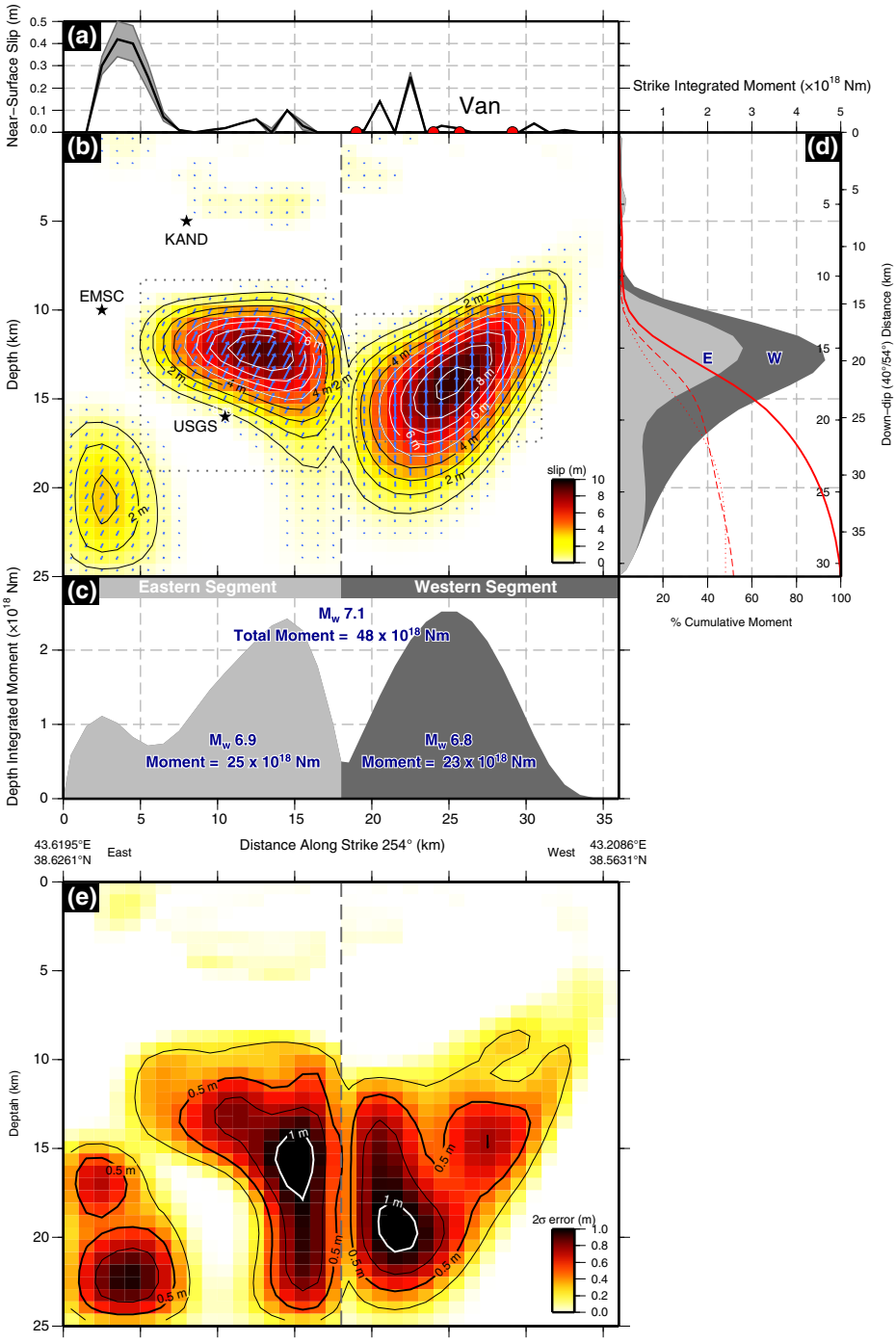

Figure 9. (a) Predicted surface offsets with 2 sigma error bounds based upon the top 1 km cell in the InSAR distributed slip model. Locations of small ground ruptures mapped in the field are denoted by red semicircles. There is only decimeter surface slip predicted within the calculated error bounds. The 40 cm surface slip in the east is considered anomalous, as it occurs beneath Lake Erçek where there are no surface InSAR constraints. (b) InSAR-derived slip distribution. Blue slip vectors indicate the motion of the hanging wall relative to the footwall. The black stars are the strike perpendicular projection of the EMSC, Kandilli Observatory (KAND), and USGS hypocenters onto the fault plane at a depth of 10, 5, and 16 km, respectively. The dashed grey box indicates the uniform slip plane extents. (c) Along strike integrated moment in each 1 km depth interval. (d) Depth-integrated moment along strike of the fault at 1 km intervals. The total cumulative moment with depth is denoted by the thick red line (the dashed line is the contribution to the moment from the eastern segment and the dotted from the western segment). Ninety-five percent of the scalar moment release occurs over the depth interval 8–20 km. (e) Two sigma error in distributed slip calculated from the standard deviation of 100 perturbed interferogram data sets based upon the atmospheric noise in each individual interferogram.

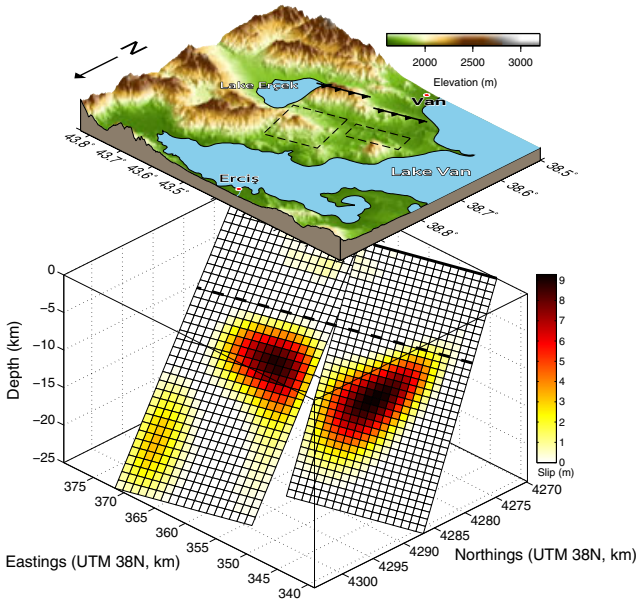

Figure 10. Perspective view of the earthquake epicenter with the up-dip fault projections marked by black/grey arrows, just north of the city of Van (top). The dashed boxes mark the outline of the slip at depth from the uniform slip model. Distribution of slip based upon the InSAR modeling (bottom). Significant slip (1 m+) occurs over the depth range 10–20 km, with almost none modeled to reach the surface. The slip on both planes ceases relatively abruptly at 9 km (dashed line), where the two fault segments cross over at depth.

(i.e., across the fault) indicates that less than 25 m of uplift has occurred across this fault zone since the terraces were deposited, translating into a maximum uplift rates of a few tenths of millimeters per year.

[35] Although detailed mapping of the terraces across the range is needed for a robust shortening rate on this fault, the calculated maximum uplift rates are low, consistent with field observations such as a fault that apparently ruptures to the surface on different splays over time. *Ozkaymak et al.* [2004], for example, report another north dipping fault exposed in Pleistocene deposits 2 km south of the western segment reported here that is on strike with the eastern segment revealed in the InSAR. Low uplift rates are also supported by the incision of the Karasu River, which has cut a valley parallel to and at the crest of the maximum uplift (Figure 8), suggesting that long-term uplift rates have been matched by Quaternary erosion rates.

[36] Despite the fluctuations in lake level shown by the terraces, the geomorphology matches the fault location: i.e., a steep, rocky coastline is seen in the hanging wall and drowned valleys in the foot-wall. This suggests that in the long term, fault movement dominates, or that the lake outlet height is buffered in some way (e.g., a sill).

4.2. Tectonics of the Turkish-Iranian Plateau

[37] The 2011 Van earthquake raises two interesting questions concerning the wider tectonics of the region. First, the event represents thrust-faulting within the high part of the Turkish-Iranian Plateau. The effects of gravitational potential energy on mountain building usually results in thrust faulting being concentrated at low elevations on the perimeters of elevated regions, with high mountains experiencing strike-slip or normal faulting [*England and Houseman*, 1986; *Copley et al.*, 2009; *Elliott et al.*, 2010]. The likely reason for the thrusting around Lake Van is suggested by the geometry of the faulting. The 2011 Van earthquake occurred at the eastern end of a band of thrust faulting extending from the Karliova Triple Junction (where the North and East Anatolian Faults meet) to Lake Van [e.g., *McKenzie*, 1972; *Saroglu and Hempton*, 1982; *Copley and Jackson*, 2006]. The north and east Anatolian faults together accommodate N-S shortening between Arabia and Asia by the westward motion of central Anatolia. In a triple junction configured in such a manner, a boundary extending eastward

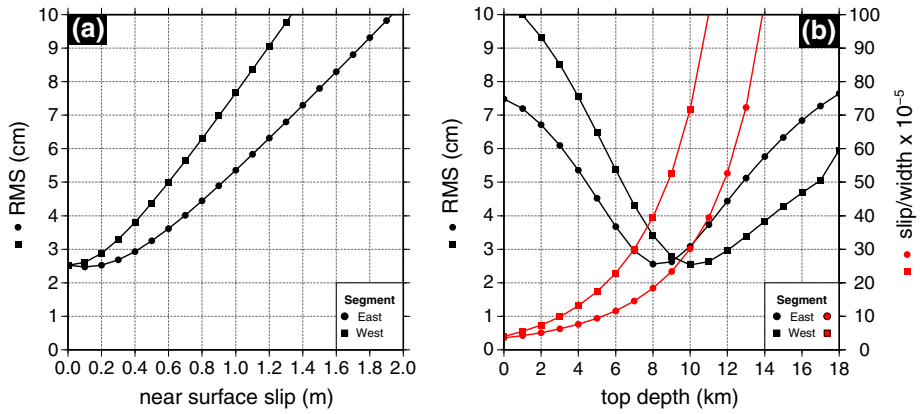

Figure 11. (a) The RMS misfit to the InSAR data for the two fault segments for varying shallow slip values 0–200 cm. The deep slip on the two fault segments is kept fixed to the best fit solutions shown in Table 1. (b) RMS well for the InSAR data with varying the top depth of each segment used in the uniform slip inversions with the slip permitted to vary (black line and dots/squares). All other parameters were fixed to the best fit solutions shown in Table 1. The RMS minimum is at a top depth of 8–10 km. Increasing or decreasing the depth of the top extent of faulting increases the RMS significantly. The red line and circles show the slip-to-fault width ratio for each solution. Top depths deeper than 10 km have unrealistically large slip-to-width ratios as the solution approaches a line source.

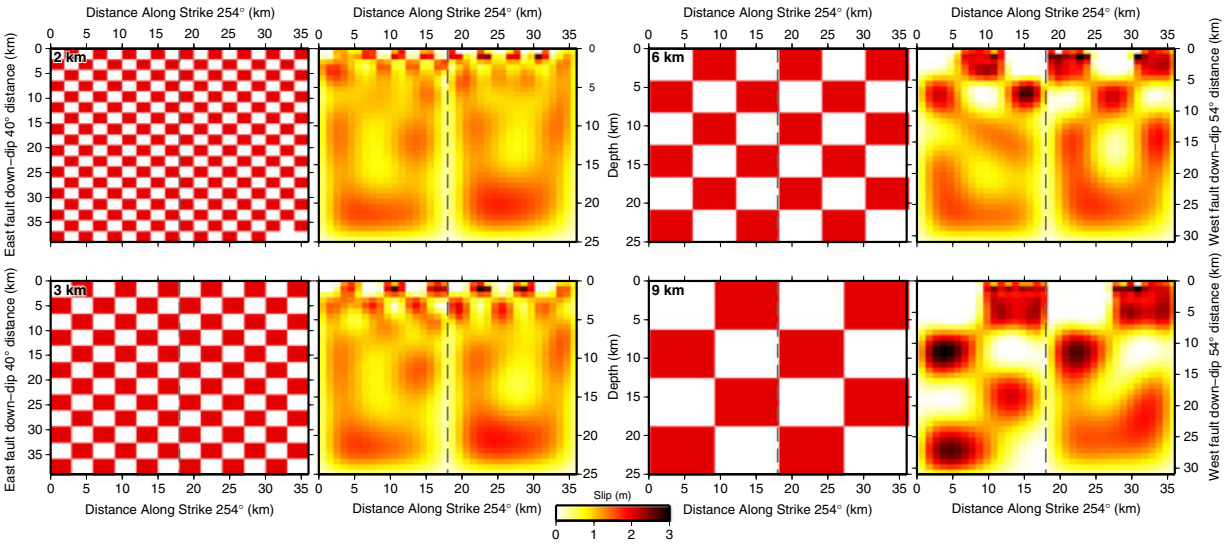

Figure 12. Checkerboard tests for a range of subfault sizes from 2 to 9 km with fixed 2 m slip patches, generated on the same two-fault segment geometry as that in the earthquake model. The resulting slip distributions are from inverting the forward models of surface deformation masked to the same coverage of SAR data and downsampled with same spatial distribution of points as that used for the real deformation data sets.

from the junction would be expected to be compressional. It is likely that thrust faulting extending from the triple junction to Lake Van performs the function of this arm of the triple junction. The existence of thrusting suggests that the stresses related to the presence of the triple junction are larger than those relating to gravitational potential energy contrasts for a distance of ∼250 km east of the triple junction, or that there was existing faulting that was easier to fail.

[38] A second point of note regarding the 2011 Van earthquake is the extent of deepest slip. Our source models show slip extending to depths of ∼20 km. The Turkish-Iranian Plateau is a region of intense volcanic activity [*Pearce et al.*, 1990], and the long-wavelength positive free-air gravity anomaly in the region [*Lemoine*, 1996] suggests this activity may be related to mantle circulation. The high geothermal gradients associated with the volcanism therefore imply that earthquakes are only likely to occur down to depths of less than 10–15 km, as observed in most other mountain ranges [*Molnar and Lyon-Caen*, 1989; *Nissen et al.*, 2011]. One possibility for the deep extent of slip in the 2011 Van event lies within the portion of the Arabian Plate that was underthrust beneath the southern margin of the Turkish-Iranian Plateau before shortening jumped north to the Greater Caucasus at 5 Ma [*Avdeev and Niemi*, 2011]. Lake Van lies at the northern edge of the region of efficient Sn propagation mapped by *Gök et al.* [2003], who suggest that the lithospheric mantle is hot or absent north of this boundary, and cooler south of it. If this boundary marks the extent of northward penetration of Arabia beneath the Turkish-Iranian Plateau, it is likely that the presence of relatively cool underthrust Arabian material would reduce the temperature of the overlying crust in the Van region and lead to seismicity at greater depths than is common for the interiors of mountain ranges (in a manner analogous to where India underthrusts southern Tibet) [*Priestley et al.*, 2008, T. J. Craig *et al.*, Thermal and tectonic consequences of India underthrusting Tibet, manuscript in review].

4.3. Fault Geometry at Depth

[39] The fault geometry and distribution of slip we find on two diverging fault planes at depth, as illustrated in Figure 10, are at odds with the classical idea of thrust fault geometries where fault segments are often thought to sole out onto a single unique fault at depth [e.g., *Suppe*, 1983]. We cannot probe the nature and geometry of the deep shear zone, nor if these diverging fault planes may join in a single structure below 25 km beneath the region of coseismic slip as measured by the surface InSAR data. The deepest limit of coseismic slip at 20–25 km likely indicates the depth of the brittle-ductile transition zone. However, we can test the robustness of the diverging fault planes in our best fit model over the depth extent from 10 km down to 20 km where the majority of the coseismic slip occurred. Our results clearly show that slip is required on relatively steeply dipping fault planes (40°–55°) in the depth range of 10–20 km. The up-dip projection of these planar segments to the surface coincides with the field fault traces and the dips also match that found in fault gouge, suggesting these faults are planar throughout the entire seismogenic depth range of the crust. The surface traces of the faults indicate that the fault is segmented along strike with a right step in faulting of about 4 km, which requires the two fault segments in the upper part of the crust.

[40] However, the deep nature of these slip sources means the surface displacement field is filtered and smoothed by the upper crust, leaving open the possibility that the COSMO-SkyMed surface displacements might be explicable in terms of a single fault plane below 9 km, with two distinct splays connecting to the surface. Therefore, we performed a distributed slip inversion model with two offset fault planes in the upper crust going down to 9 km, and

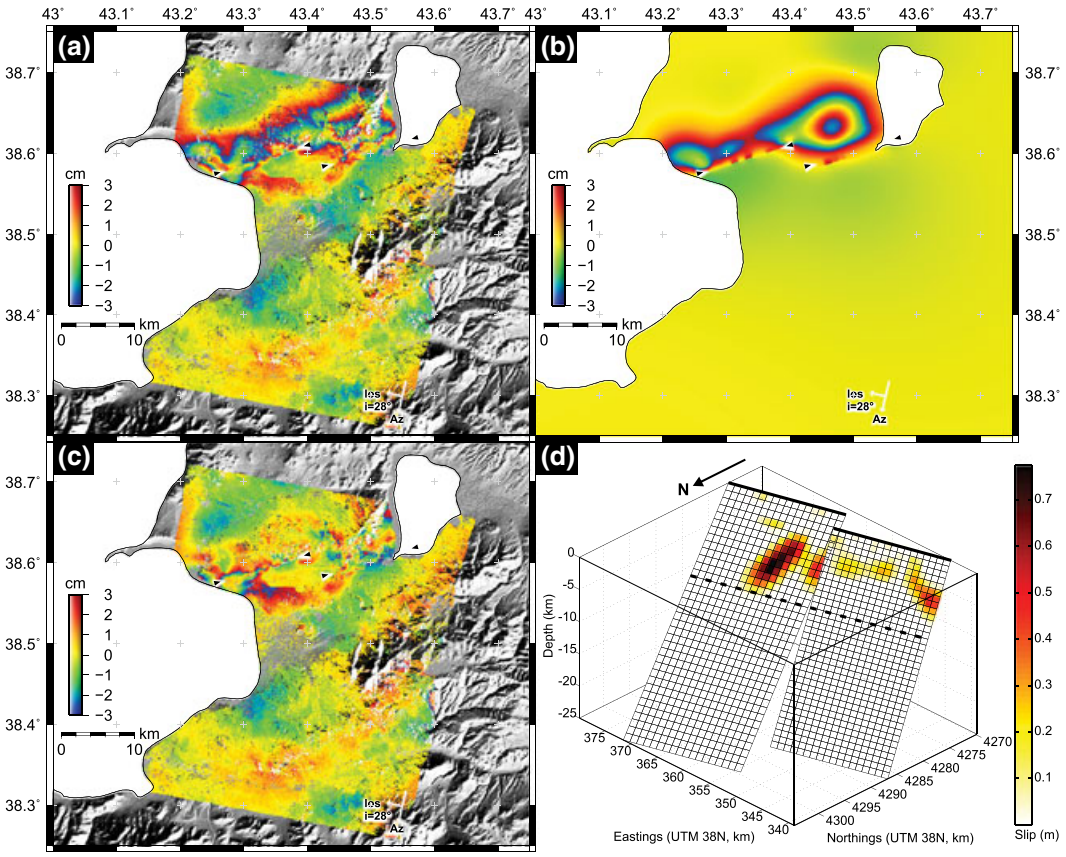

Figure 13. (a) COSMO-SkyMed postseismic interferogram formed from an acquisition 4 h after the earthquake and 3 days afterward. Black and white triangles delineate the two fault segments. A phase discontinuity is visible of the western portion, and a bulls-eye two-fringe lobe is visible just north of the eastern segment. Colors show range changes as fringes re-wrapped to 6 cm, with color cycles blue to red indicating motion away from the satellite for the three satellite tracks. Satellite track azimuth (Az) and line-of-sight (LOS) with angle of incidence (i) are shown by white arrows. (b) Model of aftershock/afterslip distribution. (c) Residuals. (d) Afterslip model from the COSMO-SkyMed postseismic interferogram, resolved on the fault planes from the main earthquake. The upper limit of rupture in the main event is delineated by the dashed line.

joining a single fault plane below 9 km (Figure 15d) that has the average dip and rake of the two upper crust planes. This is then compared to our original diverging two-plane model (Figure 15h). Whilst the depth of the slip surfaces means the models look similar in the hanging wall (Figures 15b and 15f), the residuals in the InSAR data for the deep single plane source (Figure 15c) are larger (almost double at typically 10–15 cm for the western segment) than for the diverging slip planes (Figure 15g, 5–10 cm). This is compared to a peak measured line-of-sight displacement of 90 cm. The RMS misfit between the COSMO-SkyMed InSAR data and model increases from our best fit solution of 2.1–2.6 cm for the single deep plane (Table 2). Whilst the two-planar diverging fault model (Figure 15i) provides a better fit to the data, we cannot entirely rule out the classical single plane geometry at depth for this reverse fault (Figure 15e). However, we note that in both models, two distinct slip patches are consistently found. This suggests the along-strike surface segmentation of faulting propagates to depth, indicating that fault complexity exerts some structural control on the distribution of slip.

4.4. Implications for Near-Surface Slip and Future Seismic Hazard

[41] The immediate region around Van is historically prone to earthquakes [*Ambraseys*, 1989; *Ambraseys and Finkel*, 1995], with large, destructive events having occurred previously in 1646–1648 and 1715, although the causative faults were not identified. The InSAR data presented here permit us to determine an accurate location and depth extent of faulting for the 23 October M_w 7.1 earthquake as 8–20 km, along a pair of fault planes, each ∼14 km in length. This leaves an unruptured up-dip fault width of 8–11 km (for segment dips in the range of 40°–54°). The up-dip projection of these fault segments to the surface is just 10 km north of Van. Given that the surface trace of the fault is clearly visible in the geomorphology of the mountain range to the north of Van (Figure 3) and that fault gouge was found in Quaternary sediments at the surface (Figure 4), it is very likely that the upper portion of the crust is seismogenic. The change in Coulomb stress [*Lin and Stein*, 2004] is predicted to have brought this upper section of the fault closer to failure (Figure 16). A rupture along a similar fault

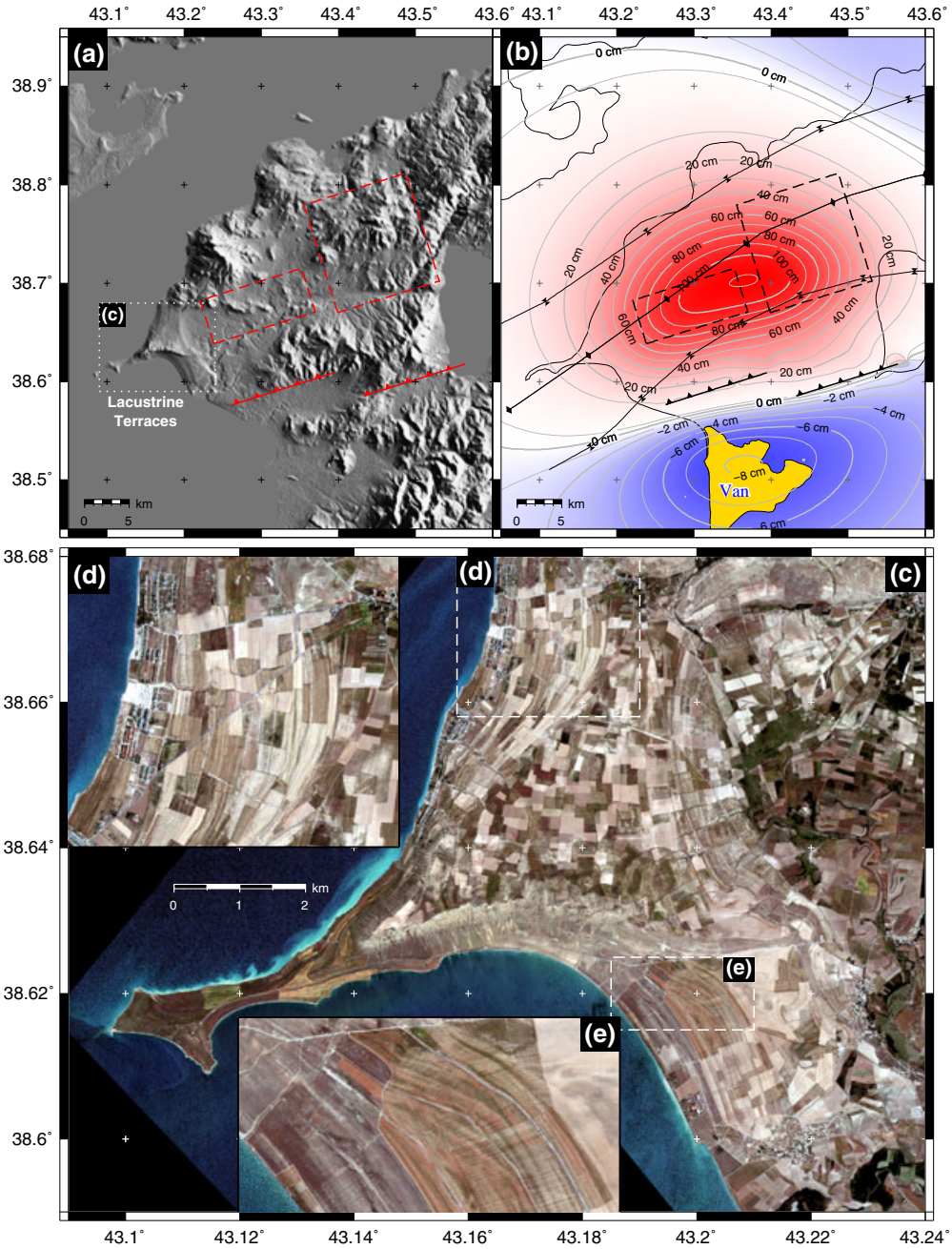

Figure 14. (a) The SRTM 90 m hill-shaded relief (illumination from the ENE). Lacustrine terraces are visible in the western shoreline as a series of three visible topographic steps. These terraces die out southward of the fault, where the shoreline enters a region of likely subsidence on the shores of the city of Van. (b) Regions of major uplift (red) and minor subsidence (blue) associated with the 23 October earthquake, based upon the dislocation model determined here from the InSAR observations. Peak uplift reaches 1.1 m. The maximum subsidence is only 8 cm in comparison. The uplift is located and aligned with the trend of the peninsula into Lake Van, as well as the trend of mapped anticline/synclines from [*Altinli*, 1966] (note some sets of anticlines/synclines running parallel to those shown have been omitted for clarity). The urban area of the city of Van is denoted by the yellow region. (c) Pan-sharpened (50 cm) WorldView-2 imagery of the shoreline northwest of the Van fault, showing lacustrine deposits and regressional terraces, with (d and e) enlargements.

length of 30 km across the remaining unruptured fault width of 10 km, with a similar average slip of 3 m, would yield a scalar moment of $\sim 3 \times 10^{19}$ Nm, equivalent to a M_w 6.9 earthquake. The shallower nature of such a rupture could potentially have a greater impact on Van.

[42] Vertical separation of slip within the seismogenic crust and a delay in rupture between two along-dip portions of a fault are known to have happened recently in the case of a pair of M_w 6.2 reverse faulting events in the Qaidam basin, NE Tibet [*Elliott et al.*, 2011]. The first earthquake occurred

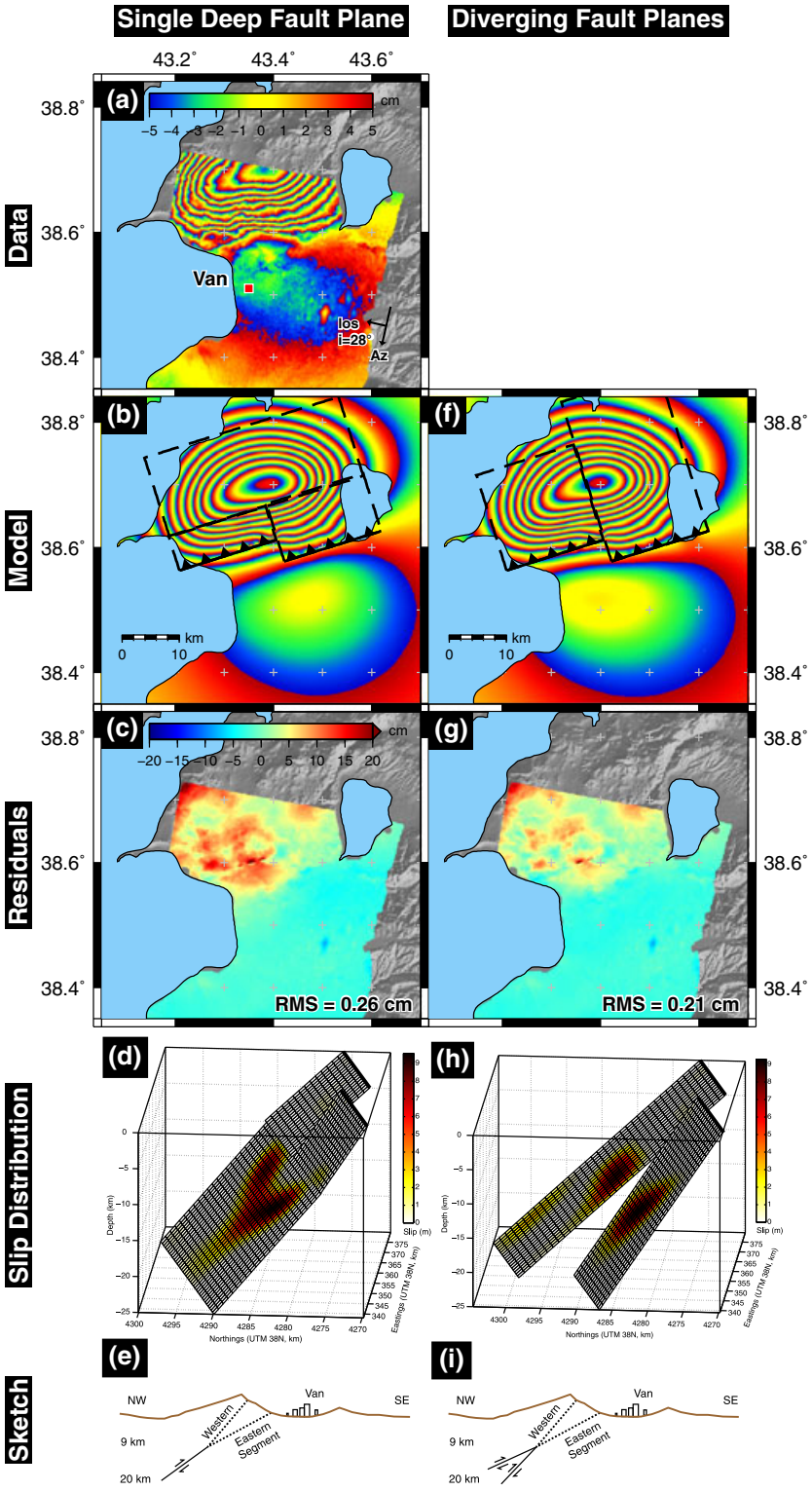

Figure 15. Comparison of the fit to the (a) COSMO-SkyMed data of (b and f) two models based upon the (c and g) residuals from the (d and h) slip distributions on two competing models of fault geometries at depth: (e) slip on a single fault plane at depth and (i) slip on two diverging fault planes.

in November 2008 with a centroid depth of 18 km. Just 10 months later, another M_w 6.2 event occurred at almost the same epicentral location, but with a centroid depth of 5 km. The InSAR data collected for this pair of events showed that they were nearly co-planar, occurring up and down dip of each other. The delay was attributed to structural depth segmentation of the seismogenic crust likely resulting from the intersection of an opposing NE dipping reverse fault plane

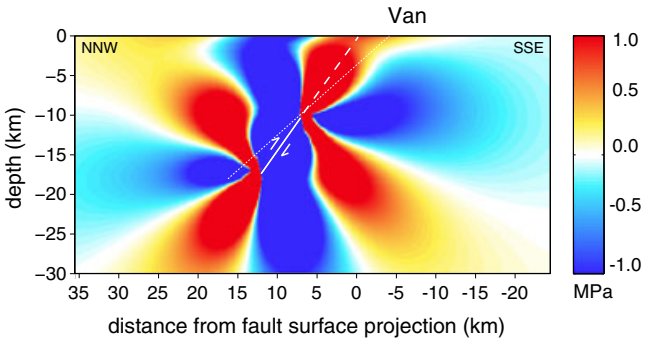

Figure 16. Cross-section of the change in Coulomb stress with depth (MPa) along a vertical profile perpendicular to the center of the western Van reverse fault segment (white line), resolved onto receiver faults with the same orientation as the causative fault. The dashed line represents the up-dip projection of the fault to the surface on which no significant slip was modeled to have occurred. The dotted line is the projection of the eastern fault segment onto the cross section. The stress changes are calculated using the Coulomb 3.1 code developed by the USGS [e.g., *Lin and Stein*, 2004].

that intersected the break in slip between these two SW dipping events [*Elliott et al.*, 2011].

[43] We have little information about possible structural complexities around Van. However, we note that the slip ceases abruptly at a depth of 9 km at which the closest ends of the two segments modeled for this event abut (Figure 10). The resolution tests (Figure 12) indicate we are able to resolve the relatively sharp boundary in slip at this depth as the slip occurs over a sufficient length scale (>6 km). Additionally, two fault slip patches are found. These two patches reflect the propagation to depth of the fault segmentation and complexity at the surface, exerting a possible structural control on the distribution of slip, although lithological changes could also be a reason [e.g., *Nissen et al.*, 2010].

[44] Another illustrative event for comparison is the 1994 Northridge M_w 6.7 reverse faulting earthquake in Southern California. The slip in this event is constrained by GPS observations to be largely below 5 km with a centroid of 10 km [*Hudnut et al.*, 1996] and lacks any clear surface trace. The two main aftershocks (M_w 6.0–6.2) which occurred the same day were thought to be located on the up-dip terminus of the mainshock rupture [*Dreger*, 1997; *Massonnet et al.*, 1996].

[45] There are also similar potential parallels between the Van earthquake and with the 1981 M_w 7.1 Sirch earthquake on the Gowk Fault in south-eastern Iran, which killed between 850 and 1500 people. Similar in size to the Van earthquake, in contrast the 1981 Sirch event did produce a surface rupture trace, yet only moderate offsets reaching the surface and a centroid depth of 18 km were found in that case [*Berberian et al.*, 1984]. Offset measurements were typically 10 cm, reaching a maximum of 40 cm. However, 17 years later in 1998, the M_w 6.6 Fandoqa earthquake with a centroid depth of 5 km re-ruptured the southern portion of the 1981 fault break, this time producing surface offsets of up to 3 m [*Berberian et al.*, 2001].

5. Conclusion

[46] We find that the Van earthquake occurred on a pair of northward dipping reverse fault planes. Slip remained buried, with peak slip of about 9 m at 14 km depth and constrained largely to the depth range 9–20 km. We perform resolution tests on the InSAR data and fault model to determine the level of robustness in the observation of a significantly large region of the up-dip portion of the fault that did not slip in this event. From this analysis, we find that an 11 km wide up-dip region remained unruptured and may pose a continuing seismic hazard to Van and the surrounding populace.

[47] **Acknowledgments.** This work was supported by the Natural Environmental Research Council (NERC) through the National Centre of Earth Observation (NCEO) of which the Centre for the Observation and Modelling of Earthquakes, Volcanoes and Tectonics (COMET, http://comet.nerc.ac.uk) is a part. AC was supported by a Research Fellowship at Pembroke College in the University of Cambridge. KS was supported in part by USAID and thanks AFAD for support during the post-earthquake field reconnaissance. Part of this work was carried out whilst JRE was a visitor at the Tectonics Observatory, Caltech, and we acknowledge Jean-Philippe Avouac and the Gordon and Betty Moore Foundation for support. All ENVISAT SAR data are copyrighted by the European Space Agency and were provided through the GEO Supersite Initiative. All COSMO-SkyMed data are purchased under license from the Italian Space Agency (ASI). WorldView data are used under license from DigitalGlobe, Inc. We thank Ruth Pottinger of Fugro-NPA for sourcing the SAR and imagery data. We are grateful to JPL/Caltech for use of the ROI_PAC software. Most figures were made using the public domain Generic Mapping Tools [*Wessel and Smith*, 1998]. We are grateful to Sue Hough and Ken Hudnut for providing USGS internal reviews on the manuscript, as well as to James Jackson for his comments.

References

Akyuz, S., C. Zabci, and T. Sancar, (2011), Preliminary Report on the 23 October 2011 Van Earthquake, *Tech. Rep.*, Istanbul Teknik Universitesi.

Albini, P., M. B. Demircioglu, M. Locati, A. Rovida, K. Sesetyan, M. Stucchi, and D. Viganò (2012), In search of the predecessors of the 2011 Van (Turkey) Earthquake, *Seismol. Res. Lett.*, *83*, 855–862, doi: 10.1785/0220110146.

Altinli, I. E. (1966), Geology of eastern and southeastern Anatolia, *Bull. Miner. Res. Explor. Inst. Turk.*, *66*, 35–76.

Ambraseys, N. N. (1989), Temporary seismic quiescence: SE Turkey, *Geophys. J. Int.*, *96*, 311–331, doi:10.1111/j.1365-246X.1989.tb04453.X.

Ambraseys, N. N. (2001), Reassessment of earthquakes, 1900–1999, in the Eastern Mediterranean and the Middle East, *Geophys. J. Int.*, *145*, 471–485, doi:10.1046/j.0956-540X.2001.01396.X.

Ambraseys, N. N., and C. F. Finkel (1995), *The Seismicity of Turkey and Adjacent Areas: A Historical Review*, 1500–1800, M.S. Eren, (Beyoglu, Istanbul).

Ambraseys, N. N., and A. Zátopek (1968), The Varto Üstükran (Anatolia) earthquake of 19 August 1966 summary of a field report, *Bull. Seismol. Soc. Am.*, *58*(1), 47–102.

Atzori, S., and A. Antonioli (2011), Optimal fault resolution in geodetic inversion of coseismic data, *Geophys. J. Int.*, *185*, 529–538, doi: 10.1111/j.1365-246X.2011.04955.X.

Avdeev, B., and N. A. Niemi (2011), Rapid Pliocene exhumation of the central Greater Caucasus constrained by low-temperature thermochronometry, *Tectonics*, *30*, TC2009, doi:10.1029/2010TC002808.

Berberian, M., J. A. Jackson, M. Ghorashi, and M. H. Kadjar (1984), Field and teleseismic observations of the 1981 Golbaf-Sirch earthquakes in SE Iran, *Geophys. J. Int.*, *77*, 809–838, doi:10.1111/j.1365-246X.1984.tb02223.X.

Berberian, M., J. A. Jackson, E. Fielding, B. E. Parsons, K. Priestley, M. Qorashi, M. Talebian, R. Walker, T. J. Wright, and C. Baker (2001), The 1998 March 14 Fandoqa earthquake (M_w 6.6) in Kerman province, southeast Iran: Re-rupture of the 1981 Sirch earthquake fault, triggering of slip on adjacent thrusts and the active tectonics of the Gowk fault zone, *Geophys. J. Int.*, *146*, 371–398, doi:10.1046/j.1365-246X.2001.01459.X.

Bird, P. (2003), An updated digital model of plate boundaries, *Geochem. Geophys. Geosyst.*, *4*(3), 1027, doi:10.1029/2001GC000252.

Copley, A., and J. Jackson (2006), Active tectonics of the Turkish-Iranian Plateau, *Tectonics*, *25*, TC6006, doi:10.1029/2005TC001906.

Copley, A., F. Boait, J. Hollingsworth, J. Jackson, and D. McKenzie (2009), Subparallel thrust and normal faulting in Albania and the roles of gravitational potential energy and rheology contrasts in mountain belts, *J. Geophys. Res.*, *114*, B05407, doi:10.1029/2008JB005931.

Daniell, J. E., B. Khazai, F. Wenzel, and A. Vervaeck (2011), The CATDAT damaging earthquakes database, *Nat. Hazard Earth Sys.*, *11*, 2235–2251, doi:10.5194/nhess-11-2235-2011.

DeMets, C., R. G. Gordon, and D. F. Argus (2010), Geologically current plate motions, *Geophys. J. Int.*, *181*, 1–80, doi:10.1111/j.1365-246X.2009.04491.X.

Dreger, D. S. (1997), The large aftershocks of the Northridge earthquake and their relationship to mainshock slip and fault-zone complexity, *Bull. Seismol. Soc. Am.*, *87*, 1259–1266.

Ekström, G., A. M. Dziewoński, N. N. Maternovskaya, and M. Nettles (2005), Global seismicity of 2003: Centroid moment-tensor solutions for 1087 earthquakes, *Phys. Earth Planet. Inter.*, *148*, 327–351, doi:10.1016/j.pepi.2004.09.006.

Elliott, J. R., R. J. Walters, P. C. England, J. A. Jackson, Z. Li, and B. Parsons (2010), Extension on the Tibetan plateau: Recent normal faulting measured by InSAR and body wave seismology, *Geophys. J. Int.*, *183*, 503–535, doi:10.1111/j.1365-246X.2010.04754.X.

Elliott, J. R., B. Parsons, J. A. Jackson, X. Shan, R. A. Sloan, and R. T. Walker (2011), Depth segmentation of the seismogenic continental crust: The 2008 and 2009 Qaidam earthquakes, *Geophys. Res. Lett.*, *38*, L06,305, doi:10.1029/2011GL046897.

Elliott, J. R., E. K. Nissen, P. C. England, J. A. Jackson, S. Lamb, Z. Li, M. Oehlers, and B. Parsons (2012), Slip in the 2010-2011 Canterbury earthquakes, New Zealand, *J. Geophys. Res.*, *117*, B03401, doi:10.1029/2011JB008868.

Emre, O., T. Duman, S. Öalp, and H. Elmaci, (2011), 23 Ekim 2011 Van Depremi Saha Gölermleri ve Kaynak Faya Ilişkin ön Değerlendirmeler, *Tech. Rep.*, Mineral Research and Exploration General Directorate of Turkey, Ankara, http://www.mta.gov.tr/v2.0/deprem/2011_Van-Depremi_On-Degerlendirmeler.pdf.

England, P., and G. Houseman (1986), Finite strain calculations of continental deformation 2. Comparison with the India-Asia collision zone, *J. Geophys. Res.*, *91*, 3664–3676, doi: 10.1029/JB091iB03p03664.

Erdik, M., Y. Kamer, M. Demircioğlu, and S. Şeşetyan (2012), 23 October 2011 Van (Turkey) earthquake, *Nat. Hazards*, *64*, 651–665, doi:10.1007/s11069-012-0263-9.

Fialko, Y. (2004), Probing the mechanical properties of seismically active crust with space geodesy: Study of the coseismic deformation due to the 1992 M_w7.3 Landers (southern California) earthquake, *J. Geophys. Res.*, *109*, B03,307, doi:10.1029/2003JB002756.

Funning, G. J., B. Parsons, T. J. Wright, J. A. Jackson, and E. J. Fielding (2005), Surface displacements and source parameters of the 2003 Bam (Iran) earthquake from Envisat advanced synthetic aperture radar imagery, *J. Geophys. Res.*, *110* (B9), B09,406, doi:10.1029/2004JB003338.

Gök, R., E. Sandvol, N. Törkelli, D. Seber, and M. Barazangi (2003), Sn attenuation in the Anatolian and Iranian plateau and surrounding regions, *Geophys. Res. Lett.*, *30*(24), 8042, doi:10.1029/2003GL018020.

Hudnut, K. W., et al. (1996), Co-seismic displacements of the 1994 Northridge, California, Earthquake, *Bull. Seismol. Soc. Am.*, *86*, S19–S36.

Jackson, J. (1992), Partitioning of strike-slip and convergent motion between Eurasia and Arabia in Eastern Turkey and the Caucasus, *J. Geophys. Res.*, *97*, 12,471–12,479, doi:10.1029/92JB00944.

Jackson, J., K. Priestley, M. Allen, and M. Berberian (2002), Active tectonics of the South Caspian basin, *Geophys. J. Int.*, *148*, 214–245, doi:10.1046/j.1365-246X.2002.01588.X.

King, G. C. P., R. S. Stein, and J. Lin (1994), Static stress changes and the triggering of earthquakes, *Bull. Seismol. Soc. Am.*, *84*(3), 935–953.

Kuzucuoğlu, C., et al. (2010), Formation of the Upper Pleistocene terraces of Lake Van (Turkey), *J. Quat. Sci.*, *25*, 1124–1137, doi:10.1002/jqs.1431.

Lemoine, F. E. (1996), The NASA and DMA joint geopotential mode, *Eos Trans. AGU*, *77*(46),

Lin, J., and R. S. Stein (2004), Stress triggering in thrust and subduction earthquakes and stress interaction between the southern San Andreas and nearby thrust and strike-slip faults, *J. Geophys. Res.*, *109*, B02303, doi:10.1029/2003JB002607.

Lohman, R. B., and M. Simons (2005a), Locations of selected small earthquakes in the Zagros mountains, *Geochem. Geophys. Geosyst.*, *6*, Q03001, doi:10.1029/2004GC000849.

Lohman, R. B., and M. Simons (2005b), Some thoughts on the use of InSAR data to constrain models of surface deformation: Noise structure and data downsampling, *Geochem. Geophys. Geosyst.*, *6*, Q01007, doi:10.1029/2004GC000841.

Massonnet, D., K. L. Feigl, H. Vadon, and M. Rossi (1996), Coseismic deformation field of the M = 6.7 Northridge, California earthquake of January 17, 1994 recorded by two radar satellites using interferometry, *Geophys. Res. Lett.*, *23*, 969–972, doi:10.1029/96GL00729.

McKenzie, D. (1972), Active tectonics of the Mediterranean region, *Geophys. J. Int.*, *30*, 109–185, doi:10.1111/j.1365-246X.1972.tb02351.X.

McQuarrie, N., J. M. Stock, C. Verdel, and B. P. Wernicke (2003), Cenozoic evolution of Neotethys and implications for the causes of plate motions, *Geophys. Res. Lett.*, *30*(20), 2036, doi:10.1029/2003GL017992.

Mitra, S. (1990), Fault-propagation folds; geometry, kinematic evolution, and hydrocarbon traps, *Am. Assoc. Pet. Geol. Bull.*, *74*(6), 921–945.

Molnar, P., and H. Lyon-Caen (1989), Fault plane solutions of earthquakes and active tectonics of the Tibetan Plateau and its margins, *Geophys. J. Int.*, *99*, 123–154, doi: 10.1111/j.1365-246X.1989.tb02020.X.

Nissen, E., F. Yamini-Fard, M. Tatar, A. Gholamzadeh, E. Bergman, J. R. Elliott, J. A. Jackson, and B. Parsons (2010), The vertical separation of mainshock rupture and microseismicity at Qeshm island in the Zagros fold-and-thrust belt, Iran, *Earth Planet. Sci. Lett.*, *296*, 181–194, doi:10.1016/j.epsl.2010.04.049.

Nissen, E., M. Tatar, J. A. Jackson, and M. B. Allen (2011), New views on earthquake faulting in the Zagros fold-and-thrust belt of Iran, *Geophys. J. Int.*, *186*, 928–944, doi:10.1111/j.1365-246X.2011.05119.X.

of Turkey Prime Ministry Disaster, R., and E. M. P. E. Department (2012), Report on Van Earthquake (Eastern Turkey).

Ozkaymak, C., T. Yurur, and O. Kose (2004), An example of intercontinental active collisional tectonics in the Eastern Mediterranean region (Van, Eastern Turkey), in *The Fifth International Symposium on Eastern Mediterranean Geology*, edited by Chatzipetros, A. A., and S. B. Pavlides, Thessaloniki.

Page, M. T., S. Custódio, R. J. Archuleta, and J. M. Carlson (2009), Constraining earthquake source inversions with GPS data: 1. Resolution-based removal of artifacts, *J. Geophys. Res.*, *114*, B01314, doi:10.1029/2007JB005449.

Pearce, J., J. F. Bender, S. E. De Long, W. S. F. Kidd, P. J. Low, Y. GiJner, F. Saroglu, Y. Yilmazm, S. Moorbath, and J. G. Mitchell (1990), Genesis of collision volcanism in Eastern Anatolia, Turkey, *J. Volcanol. Geotherm. Res.*, *44*, 189–229, doi:10.1016/0377-0273(90)90018-B.

Priestley, K., J. Jackson, and D. McKenzie (2008), Lithospheric structure and deep earthquakes beneath India, the Himalaya and southern Tibet, *Geophys. J. Int.*, *172*, 345–362, doi:10.1111/j.1365-246X.2007.03636.X.

Reilinger, R., et al. (2006), GPS constraints on continental deformation in the Africa-Arabia-Eurasia continental collision zone and implications for the dynamics of plate interactions, *J. Geophys. Res.*, *111*, 05411, doi:10.1029/2005JB004051.

Saroglu, F., and M. Hempton (1982), Tectonic and sedimentary character of the Mus-Van basin, SE Turkey, *Eos Trans. AGU*, *63*(18), 442.

Şaroglu, F., Ö Emre, and İ Kuşçu (1992), *Active Fault Map of Turkey*, General Directorate of Mineral Research and Exploration (MTA), Eskisehir Yolu, 06520, Ankara, Turkey.

Scholz, C. H. (2002), *The Mechanics of Earthquakes and Faulting*, Cambridge University Press, Cambridge.

Schweizer, G. (1975), Untersuchungen zur Physiogeographie von Ostanatolien und Nordwestiran, geomorphologische, kilma- und hydrogeographische Studien im Vansee- und Rezaiyehsee-Gebiet, Tübinger Geographische Studien, Institute of Geography, University of Tübingen.

Suppe, J. (1983), Geometry and kinematics of fault-bend faulting, *Am. J. Sci.*, *283*, 684–721.

Walker, R. T., P. Gans, M. B. Allen, J. Jackson, M. Khatib, N. Marsh, and M. Zarrinkoub (2009), Late Cenozoic volcanism and rates of active faulting in eastern Iran, *Geophys. J. Int.*, *177*, 783–805, doi:10.1111/j.1365-246X.2008.04024.X.

Wessel, P., and W. H. F. Smith (1998), New, improved version of generic mapping tools released, *Eos Trans. AGU*, *79*, 579–579, doi:10.1029/98EO00426.

Wright, T. J., Z. Lu, and C. Wicks (2004), Constraining the slip distribution and fault geometry of the Mw 7.9, 3 November 2002, Denali fault earthquake with interferometric synthetic aperture radar and global positioning system data, *Bull. Seismol. Soc. Am.*, *94*(6B), S175–189, doi:10.1785/0120040623.